Physical theory of ionomer aggregation in water

P.-É. A. Melchy and M. H. Eikerling
Simon Fraser University, 8888 University Drive, Burnaby, BC, Canada, V5A 1S6
(Received 7 January 2014; published 24 March 2014)

This article presents a physical theory for the aggregation of ionomer molecules in aqueous solution. To study this phenomenon, we consider a system of charged rigid rods with uniform surface charge immersed in water. The free-energy functional derived for this system consists of hydrophobic and direct electrostatic contributions as well as entropic terms. Energy minimization gives the stable aggregation number as a function of surface charge density, surface tension, geometric parameters, and density of rods in solution. We provide configuration diagrams of the system, which display the impact of the hydrophobic and electrostatic interaction strengths on the stabilization of finite-size bundles.

DOI: 10.1103/PhysRevE.89.032603 PACS number(s): 61.25.he, 82.45.Wx, 82.35.Rs, 82.47.Nj

I. INTRODUCTION

Charged polymers are found in a wide range of contexts, from biological systems to electrochemical devices [1]. They can be categorized according to the role of electrostatics in their properties: the behavior of polyelectrolytes in solution of high dielectric constant is governed by electrostatic interactions over distances larger than typical molecular distances, whereas ionomers are polymers with bulk properties governed by ionic interactions between discretely distributed surface groups. Ionomers are moderately charged, typically with less than 15 mol% of charged groups [2,3].

Aggregation is a major feature of charged polymers. It occurs on limited sections of the polymer, typically on the order of the persistence length. Polymers of major biological interest such as DNA or F-actin are prominent examples of polyelectrolytes; their aggregation behavior has a critical impact on their biological function. Therefore, numerous studies have investigated the underlying aggregation mechanisms of polyelectrolytes [4–13]. Oosawa's seminal polyelectrolyte model showed that like-charged rods do not attract each other if counterion fluctuations are not taken into account. Charge fluctuations due to Manning condensation [14–17] of multivalent cations, present in the electrolyte, are the key to aggregation in these systems; however, as found in these studies, thermodynamic equilibrium corresponds to an infinite bundle (see discussion in Ref. [12] and references therein), which contrasts with the observed finite-size bundles. To account for this discrepancy, kinetic arguments were put forward [11–13]. The high charge density of the condensing polyions and the multivalence of the counterions are key features of the aggregation process of highly charged polyions. Saito and Yoshikawa [18] explored a similar problem, the equilibrium of stiff polyelectrolyte rods in a monovalent salt bath, and considered the depletion force as the additional interaction governing equilibrium. They found finite-size bundles in certain regimes.

The case of ionomers aggregating in the sole presence of monovalent counterions has been studied in melts without water [19]. The case of solution with protons as counterions remains open despite its importance in such systems as the polymer electrolyte membranes (PEMs) that are used in fuel cells. Contrary to polyelectrolytes, ionomers are not charged enough for the electrostatic interaction to be the only significant interaction. If we think of uncharged hydrophobic polymers, they tend to phase separate from an aqueous solution. Hence, for an ionomer that is a copolymer with hydrophobic neutral blocks, the hydrophobicity of the neutral block provides a supplementary interaction to drive aggregation. Aggregation is thus the consequence of the interplay of electrostatic and hydrophobic interactions [17]. Understanding the conditions of ionomer aggregation in the sole presence of monovalent counterions is a nontrivial theoretical problem. Besides a theoretical interest, the problem has direct practical implications. Ionomer aggregation in water determines the physical properties of PEMs. The structure and stability of ionomer aggregates in PEMs determine water sorption [20] and stability of the membrane. These properties in turn are the key to PEM operation in polymer electrolyte fuel cells: they govern the water distribution, conductivity, and mechanical response [21].

There are numerous structural investigations of perfluorosulfonated acid (PFSA) membranes [22–25], among which Nafion remains the most widely studied material. Nevertheless, controversy persists in view of structure and properties of PEMs. Proposed models fall into two categories: Eisenberg's picture of ionic clusters [26] or structured polymer matrix models. The early model of inverted micelles based on Eisenberg's picture proposed in Refs. [27,28] has been essentially discarded. All viewpoints consider microphase separation between the backbone matrix and aqueous domains; yet they differ as to the shape of the respective phase: water channels with no clearly discernible shape amidst the polymer matrix [29], water-filled cylindrical pores [30], or fibrillar ionomer structure immersed in water [31–33]. One reason for this diversity is the loss of phase information in diffraction investigations of ionomer-water mixtures.

Another reason for the variety of experimentally backed structural models is the wide range of ionomer densities evaluated. There is evidence that PFSA membranes undergo a structural inversion from an elastic nanoporous medium at low to medium level of hydration to a gel-like network of cross-linked nanofibers in the limit of high hydration [24,30,31,34–38]. Our study focuses on the limit of dilute ionomer solutions, which is relevant for fully hydrated membranes.

In this work, we study the microscopic structure in the hydrophobic phase of PFSA membranes by developing a model of the aggregation of stiff charged rods immersed in water. In what follows, we formulate the "dry core" physical model, discuss its relevance to the aggregation of PFSA in aqueous solution, present our analysis of the model, and discuss its implications for the stabilization of PFSA membranes as compared to other membranes.

II. PHYSICAL MODEL OF AGGREGATION

A. Assumptions

In this section, we introduce the physical model of aggregation, referred to hereafter as the "dry core" model. We present the main assumptions at the outset:

(1) The local morphology of PFSA ionomers is described as stiff rods.

(2) Rods are disconnected and their set has a monodisperse distribution of lengths.

(3) Aggregates are cylindrical close-packed electrolyte-free bundles of rods.

(4) Dissociation only occurs at the surface of the bundles and the surface charge is considered as being uniform.

As for the interactions at play, we consider electrostatic and hydrophobic interactions as the driving forces that govern formation of equilibrium in this system. To solve the electrostatic problem, we employ the Poisson-Boltzmann formalism.

Let's review these assumptions and explain their origin. The morphological simplification (assumption 1) is a typical assumption made in studies of aggregation of highly charged polymers in solution [39]. It stems from the stiffness of PFSA ionomers and the local nature of aggregation. These polymers are comb-like polymers with charged groups on side chain heads as shown in Fig. 1. We can use the work [40] on neutral comb polymers to estimate the order of the radius of an equivalent tube (dotted object in Fig. 1). This yields 0.4 to 0.5 nm as an estimate. As aggregation of ionomers occurs locally, not along the whole polymer chain, we consider rigid rods. Their length L is of the order of the persistence length of the ionomer.

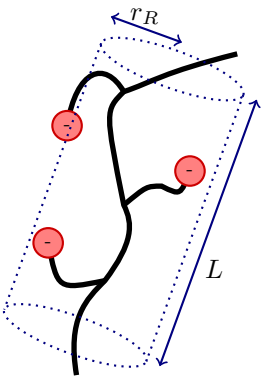

FIG. 1. (Color online) Section of Nafion ionomer and its representation as rod of radius r_R and length L. Anionic groups are depicted as red spheres. Their number is not representative: given the length L of the rods here considered, there are more of them. They are described by a continuous surface charge density σ at the surface of the rod.

Experiments using different techniques have consistently pointed at correlation lengths of the order of 300 to 500 Å [24,41,42], which is longer by a factor of 6 to 10 than for their uncharged counterpart, polytetrafluoroethylene (PTFE) [43]. In this study, we explore a range of rod lengths from 50 to 400 Å. As a consequence of this description as stiff rods, we do not explicitly take into account the side chains. As for the ionizable groups at the side chain heads, we replace them by a uniform density of ionizable groups at the surface of the rods σ_R.

Assumption (2) states that we model an ensemble of rodlike chains as a solution of stiff rods. This approximation is appropriate for a model describing local aggregation phenomena. This formalism is not suitable for larger-scale structural models. Bundles are designated by the number of rods, or aggregation number, k. We assume an ideally monodisperse distribution of aggregation numbers. The nonmonodisperse case can be described by convoluting our results with an appropriate distribution of single-rod properties.

For the calculation of the equilibrium aggregation number we use a mean-field description: the entire system is divided into cells of equal size, which each contain a single bundle in the core and the dissociated protons in the outer electrolyte shell. The ensemble of cells is replaced by a single cell with cylindrical geometry, which is concentric with the bundle in the core. The cell length is the same as the rod length, L. We neglect end effects: this approximation has been tested by varying the rod length. No dependency on the rod length is observed until getting close to the upper limit of the rod lengths describable in this mean-field approach. The radius of a cell, r_C, is a function of the density ρ of rods,

$$r_C = \sqrt{\frac{k}{\pi \rho L}}. \tag{1}$$

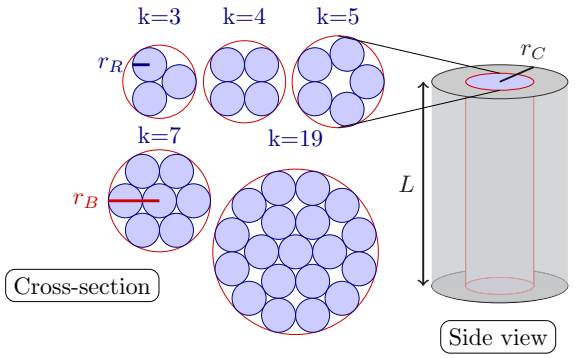

FIG. 2. (Color online) Aggregation of rod-like ionomer into k bundles with minimal radii corresponding to a given number of rods k per bundle (left). We describe the ionomer as a stiff rod with length L and with radius r_R with a continuous surface charge σ. We assume close packing of the rods into bundles. The model employs a mean-field approach: a single effective cell consists of a bundle in the core with radius r_B, surrounded by a concentric electrolyte shell with radius r_C that contains dissociated protons. Protons interact electrostatically with the uniformly charged surface of the bundle (right). Bundle cores are assumed to be electrolyte- and proton-free.

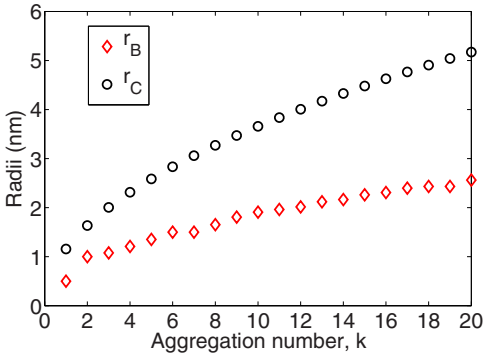

FIG. 3. (Color online) Radius r_B of the bundle and r_C of the cell as a function of the number k of rods in the bundle, using Ref. [44]. Results depicted for $L = 20$ nm and $r_R = 0.50$ nm.

Figure 2 introduces the geometric parameters of the model, and Fig. 3 depicts r_C and r_B as functions of k.

Assumption (3) stems from the strong hydrophobicity of PTFE: we consider a compact packing of the rods to minimize the interface with the aqueous solvent; the equilibrium structure of a k bundle is thus given by the close packing of k identical rods with circular cross-section in a cylinder of the same length L and with a minimal radius $r_B = r_B(k,r_R)$ to accommodate k rods of radius r_R (see Fig. 3) [44]. The dry core model assumes that the space between rods inside a bundle is electrolyte-free. This assumption is legitimate for small bundles. It implies assumption (4), that there is no dissociation of the ionizable groups of rods inside the bundle. To be deprotonated, ionizable groups have to be at the surface of the rod.

In order to simplify the equations, we consider a continuous charge density at the surface of the bundle. We write this surface charge density as

$$\sigma = \eta k \frac{r_R}{r_B} \sigma_R \,, \tag{2}$$

where σ_R is the surface charge that would be obtained at the surface of a rod if all its ionizable groups were ionized. The fraction η depends on the properties of side chains. At this stage, a precise quantitative expression of this dependency remains inaccessible. Nevertheless we can define and compare specific cases as depicted in Fig. 4. The first limiting case corresponds to zero-length side chains, $\ell_{SC} \to 0$. In this case, only ionizable groups located directly at the interface with the electrolyte dissociate. This case represents a lower bound of η in Eq. (2). The upper bound is given by the limiting case of perfect dissociation, $\eta = 1$. This situation corresponds to an ionomer with very long and flexible side chains, with all head groups protruding to the surface of the bundle. This case requires $\ell_{SC} > r_B$, an assumption that is bound to fail in a strong aggregation limit. Between these limiting cases or bounds, a continuum of intermediate cases exist, which depend on length and flexibility of side chains. Here, we evaluate the specific intermediate case with side chain length of the order of the rod radius, $\ell_{SC} \approx r_R$. This case implies that side chains that are end-grafted to rods in the outer-layer of a bundle can dissociate.

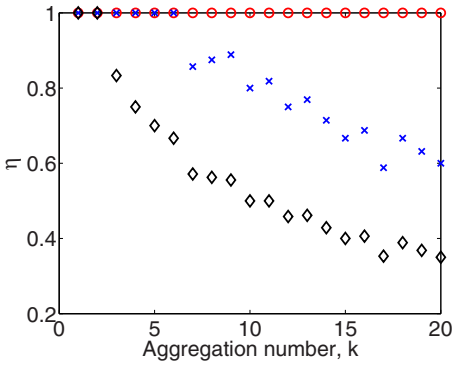

FIG. 4. (Color online) Proportion η of dissociated groups for different cases: total dissociation in the limit $\ell_{SC} > r_B$ (o), minimal dissociation in the limit $\ell_{SC} \to 0$ ($\Diamond$), and an intermediate case for $\ell_{SC} \approx r_R$ ($\times$). The value of η is calculated using the geometric parameters of the close packing of cylinders for the different dissociation scenarios [44].

B. Free-energy functional

As previously explained, ionomers are moderately charged. Backbone hydrophobicity constitutes a significant driving force for aggregation, which works together with direct electrostatic interactions to control aggregation phenomena in the system. Three kinds of electrostatic interactions exist, encompassing terms for proton-proton, proton-anionic head group and anionic head group-anionic head group interactions.

As we employ the Poisson-Boltzmann approach to solve the electrostatic problem, proton-proton interactions are not explicitly accounted for. Protons are instead described by a continuous distribution n_H. This simplifying treatment is well-suited for most problems in weak electrolytes. Charge fluctuations induced by monovalent counterions can be neglected in this problem as compared to the impact of hydrophobicity. Poisson-Boltzman equation is thus deemed sufficient to describe the electrostatic problem. The linearized version of this equation is widely adopted in case of a weak electrolyte thanks to compensating approximations it entails [45]. This is the reason why it can be employed even for polyelectrolytes. The most prominent example is the use of the Debye-Hückel theory to describe electrostatic interactions between biological macroions and more specifically DNA [46].

The electrostatic interaction between dissociated protons and charged anionic groups at rod surfaces causes a net repulsive interaction between rods. This contribution is given by the electrostatic energy of the proton distribution n_H in a cylindrical cell that contains a bundle with a correspondingly negatively charged surface at equilibrium. For hydrophobic interaction terms, we use an interfacial energy determined by the surface tension. We approximate the interfacial area by the area of the bundle cylinder.

Hence, the free-energy density of a k bundle in its cylindrical cell is

$$f(k) = L\rho(\tilde{f}_k - \tilde{f}_1) - T(s_k - s_1). \tag{3}$$

The entropy s_k per k bundle is given by

$$s_k = -\rho_0 k_B [x_k \ln x_k - (1 + x_k) \ln(1 + x_k)], \tag{4}$$

where x_k stands for the k bundle molar fraction with reference to the solvent (water in this case), that is $x_k = \rho/(k\rho_0)$ with $\rho_0 = 33.12\ \mathrm{nm}^{-3}$. The free energy is written with reference to the single-rod limit, $\tilde{f}_1$, considered to be a baseline of fixed energy. $\tilde{f}_k$ is the contribution per rod and per unit length of a bundle in an isolated cell,

$$\frac{k\tilde{f}_k}{2\pi} = r_B\gamma - r_B\frac{\sigma}{q}E_{\mathrm{solv}} + r_B\int_0^{\sigma} d\sigma'\varphi_{r_B}(\sigma') + q\int_{r_B}^{r_C} r dr\,\varphi(r)n_H(r), \tag{5}$$

where γ is the coefficient of surface tension, φ is the potential created by the k bundle, and n_H is the proton-density distribution in the cell. The first term on the right-hand side of Eq. (5) accounts for hydrophobic interactions; the second term accounts for the anion solvation energy; the third term expresses the electrostatic repulsion between rods as the energetic cost to build the bundle surface with a surface charge σ (similarly to the definition of a work function); the last term is the electrostatic interaction between the k bundle and the dissociated protons in the cell.

To evaluate the free energy, we calculate the electrostatic potential φ and the proton distribution. We consider the limit of low-charge densities, which yields the following expression of proton density:

$$n_H(r) = n_H^0\exp(-q\beta\varphi) \approx n_H^0(1 - q\beta\varphi), \tag{6}$$

where q is the elementary charge, $\beta^{-1} = k_BT$, and we obtain

$$\nabla^2\varphi - \kappa^2\varphi = -\frac{4\pi q n_H^0}{\varepsilon}, \tag{7}$$

where the inverse Debye length κ is defined by $\kappa^2 = 16\pi^2 n_H^0\ell_B$, with the Bjerrum length defined as $\ell_B = q^2\beta/(4\pi\varepsilon)$.

At the surface of the bundle, at $r = r_B$, the electric field is related to the surface charge density via Gauss' law. At the boundary of the cylindrical cell, the cell model approximation requires that the electric field is zero. Therefore, the boundary conditions are

$$\hat{e}_r(\varepsilon_{\mathrm{ext}}\vec{\nabla}\varphi_{\mathrm{ext}}|_{r=r_B} - \varepsilon_{\mathrm{int}}\vec{\nabla}\varphi_{\mathrm{int}}|_{r=r_B}) = -4\pi\sigma, \tag{8}$$

$$\vec{\nabla}\varphi(r = r_C) = 0. \tag{9}$$

In this case, the solution to Eq. (7) is

$$q\beta\varphi(r) = 1 + \frac{4\pi q\beta\sigma}{\varepsilon\kappa}\tilde{\Delta}(r), \tag{10}$$

where

$$\tilde{\Delta}(r) = \frac{K_1(\kappa r_C)I_0(\kappa r) - I_1(\kappa r_C)K_0(\kappa r)}{I_1(\kappa r_C)K_1(\kappa r_B) - I_1(\kappa r_B)K_1(\kappa r_C)}, \tag{11}$$

with I_n and K_n being modified Bessel functions of the first and second kind. Thus, the proton distribution in Eq. (6) is

$$n_H(r) = -\frac{4\pi\sigma}{\varepsilon\kappa}q\beta n_H^0\tilde{\Delta}(r). \tag{12}$$

TABLE I. List of system parameters.

Parameters	Baseline	Value range used in this work
γ	4.0 eV nm^{-2}	2.0 eV nm^{-2} to 4.0 eV nm^{-2}
σ	-0.5 (e) nm^{-2}	-0.5 (e) nm^{-2} to -1.0 (e) nm^{-2}
ρ	1.19×10^{-2} nm^{-3}	
ε_r	55.3	55.3
T	373 K	373 K
r_R	0.5 nm	0.25 nm to 0.70 nm
L	20 nm	5 nm to 40 nm
E_{solv}	-0.2 eV	-0.1 to -0.4 eV

To evaluate the normalization constant, we employ the condition of electroneutrality of the cell,

$$L\int_{r_B}^{r_C} r dr n_H(r) = r_B L\frac{|\sigma|}{q}. \tag{13}$$

This induces a self-consistent loop to calculate n_H^0 defined by

$$n_H^0 = \frac{r_B^2}{16\pi^2\ell_B\left[\int_{r_B}^{r_C} r dr\tilde{\Delta}(r)\right]^2}. \tag{14}$$

We initialize this self-consistent calculation by using the homogenous limit,

$$n_H^{\mathrm{init}} = \frac{2\sigma}{qr_B\left[1 - \left(\frac{r_C}{r_B}\right)^2\right]}. \tag{15}$$

C. Parameters: Baseline case

Regarding the dissociation factor introduced in Eq. (2), the baseline is defined as the intermediate case. We consider the system at $T = 373$ K and assume an aqueous solution with $\varepsilon_r = 55.3$. As for the parameters defining the strength of the interactions, we chose the baseline to correspond to Nafion. For the surface tension we use the value of Teflon, $\gamma = 4.0$ eV nm^{-2}, as a reference. The reference surface charge density is $\sigma = -0.5$ (e) nm^{-2}, where, as in Table I, the notation (e) denotes "in the units of the elementary charge e." This value of σ corresponds to an ion exchange capacity of 0.9 meq g^{-1}. For the density of rods, we use a typical value for Nafion membrane, $\rho = 1.19\times10^{-2}$ nm^{-3}. We use the solvation energy calculated for triflic acid [47] as a reference and thus employ a value of $E_{\mathrm{solv}} = -0.2$ eV as the baseline. The remaining geometric parameters are extracted from experiments (rod length) and theoretical considerations (rod radius). Table I summarizes the baseline case as well as the range of values explored in this study. The plots and results presented in Sec. III will refer to the baseline case unless otherwise stated.

III. RESULTS

A. Free-energy functional minimization

Since we investigate the aggregation properties through the minimization of the free-energy functional introduced in Eq. (3), we start this section by discussing the shape of the free energy as a function of bundle size. Different cases exist. The functional can be decreasing on the whole range of bundle size

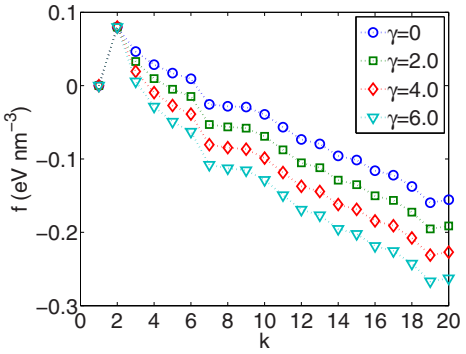

FIG. 5. (Color online) Free energy plotted as a function of aggregation number for different surface tensions in the case of perfect dissociation, $\ell_{SC} \gg r_R$. As can be seen, the free energy is a decreasing function, which implies relaxation toward a phase-separated state.

considered as shown in Fig. 5. In this case the system is driven to complete phase separation. Figure 6 displays a case with increasing free energy for the largest values of the surface charge density σ. In this case, the equilibrium is a solution of dispersed rods. In between these limiting cases, there is a region of the parameter space for which the functional is flat and shallow. In this case, equilibration can be expected to be a rather slow process and thermal excitation should give rise to a statistical distribution of structural conformations of bundles with similar energy. This behavior can be inferred from results seen in Figs. 6 and 7.

B. Dissociation

Here we discuss the limiting cases of dissociation, defined in Sec. II A (see Fig. 4). In the limit of perfect dissociation, which corresponds to $\eta = 1$ in Eq. (2), we can observe that the free energy decreases as the aggregation number increases, for any combination of surface charge density and surface tension, as in Fig. 5. As a result, the system, in this limit, will always approach a perfectly phase-separated state. As such this limit is unphysical: side chains have finite lengths; it is thus impossible

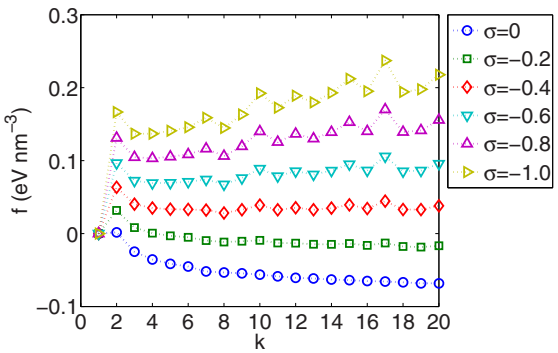

FIG. 6. (Color online) Free energy plotted as a function of aggregation number for different surface charge densities in the case of minimum dissociation, $\ell_{SC} \to 0$. As the surface charge density increases, the free energy moves toward positive values. Moreover, a metastability can be observed at the transition with different configurations on the zero-energy manifold.

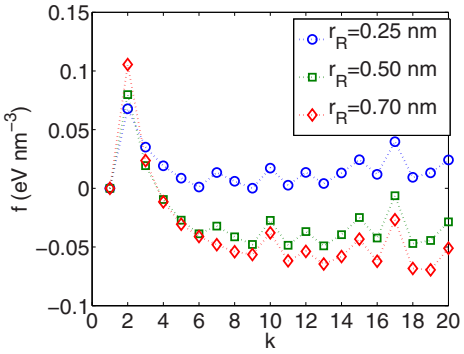

FIG. 7. (Color online) Free energy for different radii r_R.

for all ionizable groups to protrude to the surface of the bundle, irrespective of the bundle size. Perfect dissociation with $\eta = 1$ could be achieved only for bundles with radius below a critical value.

In the limit of minimal dissociation, the analysis of the free energy as a function of aggregation number reveals that there are two equilibrium configurations: either a phase separated system or a system of dispersed rods. If we look at Fig. 6, we can see that the free energy is a decreasing function of bundle size for nontrivial bundles ($k \geqslant 2$) at low surface charge densities. At sufficiently high surface charge density, $|\sigma| \gtrsim 0.4\,(e)\ \mathrm{nm}^{-2}$, the free energy becomes a monotonously increasing function of bundle size. It moves toward positive values and becomes mostly increasing as the surface charge density increases. In other words, the equilibrium changes from a phase separated system at low surface charge density to a solution of dispersed rods at high surface charge density. This trend is expected as it corresponds to an evolution from a system dominated by hydrophobicity to one governed by repulsive electrostatic interactions. The transition occurs when the free energy crosses the zero-energy level for aggregation numbers $k \geqslant 2$. Interestingly, at the transition, as the free energy is mostly convex for $k \geqslant 2$, there is metastability with different aggregation numbers belonging to the zero-energy manifold.

C. Impact of geometrical parameters

Figures 7 and 8 display the impact of the rod radius on the equilibrium bundle size. The overall trend is that the aggregation number increases with r_R. This dependence is continuous and more pronounced for a smaller absolute value of the ion solvation energy, $E_{\mathrm{solv}} = -0.2$ eV, as illustrated in Fig. 8(a). At the value $E_{\mathrm{solv}} = -0.3$ eV, shown in Fig. 8(b), bundle formation does not occur for $r_R \leqslant 0.6$ nm as the penalty for ion solvation is too high.

As previously explained, for the sake of relevance to the aggregation in PFSA membranes, we focus on $5 \leqslant L \leqslant 40$ nm, consistent with the following condition,

$$L \ll L^k_{\mathrm{lim}} = \frac{k}{\pi \rho r_B^2}, \tag{16}$$

where L^k_{lim} is a limit imposed by geometric considerations. This condition is equivalent to imposing $r_B \ll r_C$, which is a condition for the cell model to be a valid approximation.

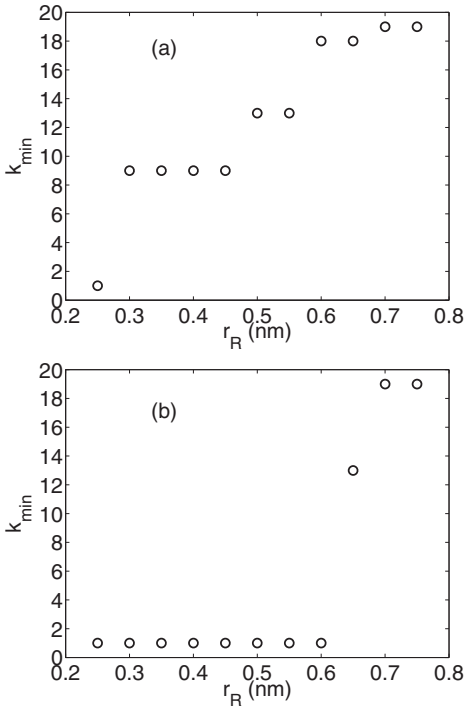

FIG. 8. Equilibrium size of bundles for different rod radii r_R with baseline case parameters. The solvation energy is: (a) $E_{\text{solv}} = -0.2$ eV and (b) $E_{\text{solv}} = -0.3$ eV.

Figure 9 shows L_{lim} for a reference rod density of $\rho = 1.19 \times 10^{-2}$ nm^{-3}. It appears that L^k_{lim} depends strongly on r_R. If we want to be able to describe rods with $L = 40$ nm we should have $r_R < 0.7$ nm.

In Fig. 10, a sharp drop of the equilibrium bundle size occurs around $L_{\text{lim}} \approx 40$ nm. Below this value there is a small range of increase of the equilibrium bundle size but further away from this upper limit of validity of the cell model, the equilibrium bundle size is remarkably stable, which indicates that end effects can be neglected.

Another important parameter controlling stable bundle sizes is the density of rods, ρ (Fig. 11). In the limit of dilute systems (the lowest density we investigated was $\rho = 5.0 \times 10^{-5}$ nm^{-3}), the free energy flattens, indicating that

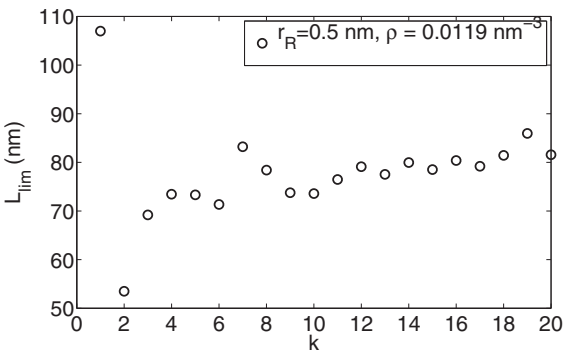

FIG. 9. Upper bound L^k_{lim} for the length of the rods as a function of the size k of the bundle. Depicted for the reference density $\rho = 1.19 \times 10^{-2}$ nm^{-3} and the radius $r_R = 0.50$ nm.

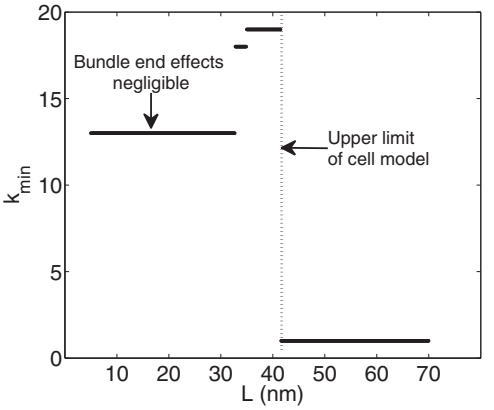

FIG. 10. Bundle equilibrium size as a function of rod length L.

the relaxation to equilibrium slows down with dilution. For $\rho < 0.02$ nm^{-3}, the mean distance of rods in a dispersed solution is larger than the Bjerrum length ℓ_B. Equilibration processes are thus slowed down as electrostatic interactions are weakened.

Similarly to what happens for the rod length, around the upper limit of validity of the cell model, the equilibrium bundle size increases before plunging to $k_{\text{min}} = 1$, which indicates the breakdown of the mean-field approximation. The critical value of the density derives from the inequality introduced in Eq. (16).

D. Dependence on surface tension and charge density

In this subsection, we discuss the stable size of bundles, i.e., the number of rods per bundle at equilibrium, as a function of surface tension γ and surface charge density σ. This information is displayed in the form of configuration diagrams, shown in Fig. 12.

The system exhibits diverging aggregation numbers in the limit of vanishing surface charge density. In this limit of negligible electrostatic interactions, hydrophobic interactions drive the system toward complete phase separation. The entropic component of the free energy introduced in Eq. (3) is independent of surface charge density. As for the internal

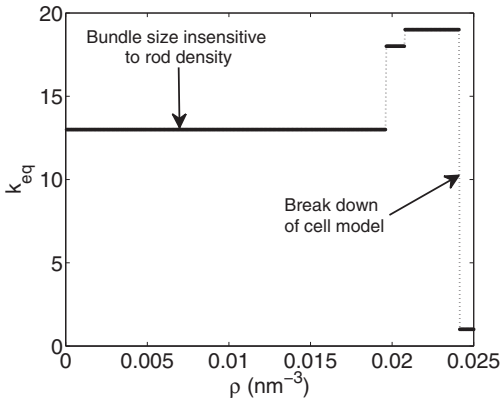

FIG. 11. Equilibrium aggregation number as a function of rod density ρ.

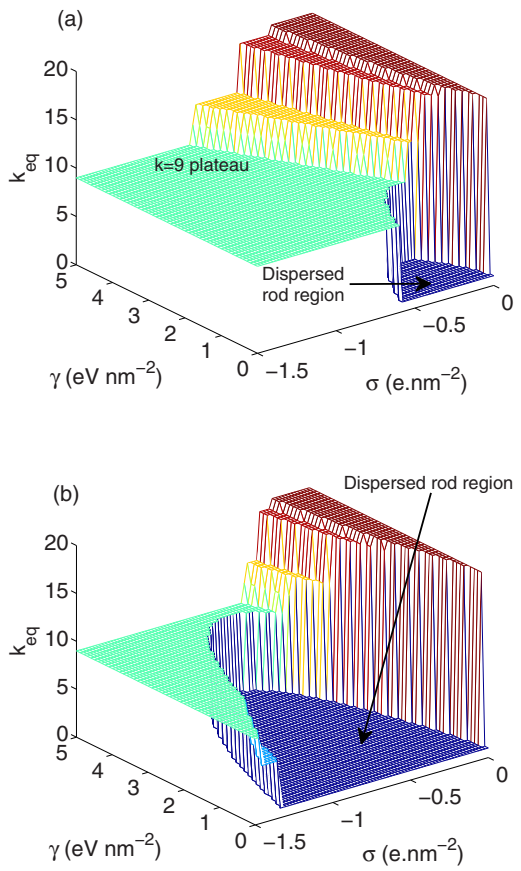

FIG. 12. (Color online) Configuration diagram for the baseline case, except the solvation energy, which is (a) $E_{\rm solv} = -0.2$ eV, respectively, (b) $E_{\rm solv} = -0.3$ eV. The equilibrium bundle size is reported along z axis.

energy, Eq. (5), it can be written anew as follows:

$$\frac{k\tilde{f}_k}{2\pi} = \left[\gamma + \frac{4\pi}{\varepsilon\kappa}\tilde{\Delta}(r_B)\sigma^2 + \left(\frac{1}{q\beta} - \frac{E_{\rm solv}}{q}\right)\sigma\right] r_B + q\int_{r_B}^{r_C} r dr\, \varphi(r) n_H(r). \quad (17)$$

This form reveals that all contributions but the hydrophobic one scale with the surface charge σ, or positive powers of it.

Another visible limit in this configuration diagram is the dispersed rod region. It corresponds to the region where electrostatic interactions dominate. Indeed, if there were only electrostatic interactions, aggregation could not occur as the counterions are monovalent. It is normal to reach this limit in a sector where surface tension is weak in comparison to electrostatic interaction terms. The boundary of this dispersed-rod domain prescribes a parabolic curve as implied in Eq. (17). When $\gamma = 0$, the dispersed rod state exists over a certain range of σ. Increasing γ, the last term in Eq. 17 is not affected and the level sets of the first term in square brackets are exactly parabolic in (γ,σ) space. Hence, within the parabola defined by the level set corresponding to the limit of stability of the dispersed rod at $\gamma = 0$, the dispersed rod state minimizes the free energy. For increasing $E_{\rm solv}$, the parabolic domain expands to a wider range of $|\sigma|$ values and a larger apex value along the γ axis. This is clearly visible when comparing Figs. 12(a) and 12(b), for $E_{\rm solv} = -0.2$ eV and $E_{\rm solv} = -0.3$ eV, respectively.

Between the limit of complete phase separation and the single rod limit, a cascade of intermediate configurations exist. The largest domain corresponds to 9-bundles (light green in the online colored version of Fig. 12). This configuration presents eight rods at the surface and one rod in the center. If the energy of solvation were so strong as to impose full dissociation, the equilibrium aggregation number would be $k = 6$, which corresponds to the largest single-layer bundle. For $k_{\rm eq} = 9$, the solvation energy still imposes very high dissociation, but the hydrophobicity requires to minimize more the interfacial area between bundles and water. These configurations lead to the formation of a close-packed bilayer-type configuration that maximizes dissociation with eight out of nine rods at the surface of the bundle. These geometric remarks provide an intuitive understanding and a rule of thumb to predict trends as side chain length changes. Upon increasing side chain length, the equilibrium aggregation number shifts toward larger values. For $\ell_{\rm SC} \approx 2r_R$, we can expect bundles with two or three layers as the most stable configurations, namely $k = 19$ and $k = 20$. These expectations still need to be further tested experimentally. The available SAXS and SANS data for Nafion, Hyflon, and Aciplex [48,49] are not conclusive in view of the precise characteristics of stable bundles. Local probes, such as atomic force microscopy, might prove more insightful in this regard.

IV. DISCUSSION

The results presented in this paper warrant a number of comments. First, the limit of perfect dissociation represents an unphysical limit as the assumption of side chain head groups protruding to the surface of the bundle, whatever the size of a bundle, cannot hold. To explore the limit of near perfect dissociation one of the basic assumptions of the model needs to be challenged, namely the absence of electrolyte inside the bundle. Given the large difference of dielectric constant between aqueous solution (55.3) and ionomer (typically about 2), we can expect a quasineutralization of the charges inside the bundle leaving an effective surface charge at the external interface between the bundle and the aqueous solution [50]. Such calculations would thus bring back a system similar to the one here studied, albeit with a significantly reduced portion of dissociated and mobile protons.

The proposed theoretical formalism draws attention to a major structural correlation effect. It refers to the correlation between the degree of ionomer dissociation and the effective length of side chains. The proposed treatment of different dissociation regimes in this paper is a coarse approach to incorporate this correlation, but it allows relevant conclusions for the impact of the lengths of side chains on ionomer aggregation to be drawn.

The self-assembly of rigid ionomer molecules into aggregates with cylindrical geometry emerges as a consistent scenario from the theoretical analysis. These aggregates form the microscopic building blocks of the membrane skeleton. Primary tests for the validity of this conclusion are studies of ionomer aggregation in dilute solution. Indeed, formation of cylindrical aggregates was found experimentally in Nafion solution. Aggregate radii determined from diffraction

experiments, using small-angle neutron or x-ray scattering (SANS or SAXS) [24,34,51–53], as well as spectroscopic measurements using electron spin resonance (ESR) [54,55], are in the range of 15 to 25 Å, which compares well with results of our theory.

Furthermore, experimental studies showed that the radius of cylindrical aggregates in solutions of short side chain PFSA ionomers is smaller than in solutions of long side chain PFSA ionomers [34]. This result agrees with the trend predicted on the basis of the theory: longer side chains result in larger equilibrium bundle size.

Studies of ionomer aggregation in the dense ionomer limit, corresponding to membrane formation, are more precarious. Nevertheless, we maintain a claim that cylindrical aggregates represent the primary structural motif, from which complex statistical structures of PEMs are formed. Atomic force microscopy results support this claim [56]. Gebel and coworkers have carried out analyses of SANS and SAXS measurements for PFSA ionomer membranes [31–33]. From the scaling law for the scattering intensity as a function of the wave number, $I(q) \propto q^{-1}$, which is characteristic of cylindrical structures, they concluded that cylindrical polymer aggregates are the building blocks of membranes.

However, the interpretation of scattering data for water-filled PEMs remains controversial [30,32,57]. Plots of the free energy of ionomer bundles as a function of aggregation number, shown in Fig. 7, could partly explain this lasting controversy. The free energy minima are shallow and there is a quasidegeneracy of bundles with different aggregation numbers, due to small energy differences (in the order of $k_B T$) associated with transitions between bundle sizes. Thus, a free-energy minimum can be well-defined at the microscopic scale for a single bundle, but for a macroscopic ensemble of bundles it seems unreasonable to predict a stable configuration on the basis of free-energy considerations. By the same argument it appears futile trying to identify a prevailing shape of pores. A PEM is expected to exhibit a random statistical distribution of bundle sizes and pore shapes. However, at the macroscopic scale, a PEM does not relax to a structurally well-defined state. This reasoning could explain why membrane fabrication and pretreatment methods have such a vital impact on PEM structure and properties.

Atomistic molecular dynamics (MD) have consistently been unable to rationalize the aggregation of backbones in PFSA systems [58–61]. The reason is the extremely slow relaxation in these systems [62]. As noted in Ref. [59]: finding the equilibrium microstructure when starting with a totally random distribution of polymer chains in the simulation box is prohibitive due to insufficient simulation times. For the same reason, coarse-grained simulation approaches, such as coarse-grained molecular dynamics or dissipative particle dynamics [63,64], have been unable to address this problem. Moreover, the microscopic aggregation is absent from the computational framework that is based on self-consistent mean field theory [65,66]. A way to overcome the limitation of short computable time scales is to start with preconstrained systems, similarly to what was done in Ref. [59]. Following this approach, different morphological models for microscopic structures could be evaluated and compared. Thereby, distributions of bundle sizes could be investigated further.

We can compare our results with other works that explored the aggregation of charged polymers using approaches based on minimization of free-energy functionals. In Ref. [18], the authors explored aggregation of polyelectrolytes in a monovalent salt bath of stiff charged rods with small surface tension. They found an equilibrium bundle radius of $r_B = 9$ nm for $\gamma\beta^{-1} = 0.197$ nm^{-2}. These bundle radii correspond to aggregation numbers of $k = 40$–80. The equilibrium bundle sizes are, therefore, much larger than those found in our work; the main reason for the large discrepancy is the screening of electrostatic interactions by salt ions within the bundle. In their work, the authors also found an increase of equilibrium aggregation number upon the increase of the surface tension, similar to our results. In the absence of hydrophobicity they found no aggregation, as expected.

V. CONCLUSION

We have studied the stability of bundles of ionomer molecules to investigate microscopic aggregation phenomena in solutions of PFSA ionomer molecules. Ionomers were described as rigid rods with uniform surface charge density. The discrete distribution of ionomer side chains was not explicitly accounted for. The impact of the length of side chains was evaluated by implicitly comparing different dissociation scenarios.

A free-energy functional developed for this system accounts for direct electrostatic as well as hydrophobic interactions. The model proves sufficient to describe the formation of microscopic cylindrical bundles observed in dilute solutions of typical PFSA materials. Bundles are characterized by their aggregation number, which is sensitive to the density of acid groups along the ionomer backbone and to the surface tension of hydrophobic backbone segments. Predicted trends for the variation of bundle sizes with these parameters are consistent with experimental studies on ionomer aggregation in solution.

We claim that cylindrical bundles of ionomer backbones are the prevailing structural motif in ionomer membranes. However, the small energy differences between bundles of varying size imply that a membrane exhibits random statistical distributions of bundle sizes as well as of shapes and sizes of pores enclosed by such bundles. Rationalizing these distributions will be essential in order to understand elastic properties, water sorption behavior, and transport properties of PEMs.

ACKNOWLEDGMENTS

This project is supported by an Automotive Partnership Canada grant and by Ballard Power Systems.

[1] M. Hara, *Polyelectrolytes: Science and Technology* (Marcel Dekker, New York, 1993).

[2] Edited by S. Schlick, *Ionomers: Characterization, Theory, and Applications* (CRC Press, Boca Raton, 1996).

[3] A. Eisenberg and J.-S. Kim, *Introduction to Ionomers* (John Wiley & Sons, New York, 1998).
[4] F. Oosawa, Biopolymers **6**, 1633 (1968).
[5] S. L. Brenner and D. A. McQuarrie, J. Theor. Biol. **39**, 343 (1973).
[6] S. L. Brenner and D. A. McQuarrie, J. Colloid Interface Sci. **44**, 298 (1973).
[7] S. L. Brenner and D. A. McQuarrie, Biophys. J. **13**, 301 (1973).
[8] V. A. Bloomfield, Biopolymers **31**, 1471 (1991).
[9] R. Marquet and C. Houssier, J. Biomol. Struct. Dyn. **9**, 159 (1991).
[10] J.-L. Barrat and F. Joanny, in *Advances in Chemical Physics: Polymeric Systems*, Vol. XCIV, edited by I. Prigogine and S. A. Rice (John Wiley & Sons, Inc., New York, NY, 1996), Chap. 1, pp. 1–66.
[11] B.-Y. Ha and A. J. Liu, Phys. Rev. E **58**, 6281 (1998).
[12] B.-Y. Ha and A. J. Liu, Europhys. Lett. **46**, 624 (1999).
[13] M. L. Henle and P. A. Pincus, Phys. Rev. E **71**, 060801 (2005).
[14] G. S. Manning, J. Chem. Phys. **51**, 924 (1969).
[15] G. S. Manning, J. Chem. Phys. **51**, 934 (1969).
[16] G. S. Manning, J. Chem. Phys. **51**, 3249 (1969).
[17] G. Manning, Eur. Phys. J. E **34**, 1 (2011).
[18] T. Saito and K. Yoshikawa, J. Chem. Phys. **133**, 045102 (2010).
[19] D. S. Bolintineanu, M. J. Stevens, and A. L. Frischknecht, Macromolecules **46**, 5381 (2013).
[20] M. H. Eikerling and P. Berg, Soft Matter **7**, 5976 (2011).
[21] W. Vielstich, A. Lamm, and H. A. Gasteiger (eds.), *Handbook of Fuel Cells: Fundamentals, Technology, and Applications* (Wiley, New York, 2003).
[22] K. A. Mauritz and R. B. Moore, Chem. Rev. **104**, 4535 (2004).
[23] K.-D. Kreuer, Chem. Mater. **8**, 610 (1996).
[24] G. Gebel, Polymer **41**, 5829 (2000).
[25] D. Liu, S. Kyriakides, S. W. Case, J. J. Lesko, Y. Li, and J. E. McGrath, J. Polym. Sci., Part B: Polym. Phys. **44**, 1453 (2006).
[26] A. Eisenberg, Macromolecules **3**, 147 (1970).
[27] W. Y. Hsu and T. D. Gierke, Macromolecules **15**, 101 (1982).
[28] W. Y. Hsu and T. D. Gierke, J. Membr. Sci. **13**, 307 (1983).
[29] K. Kreuer, J. Membr. Sci. **185**, 29 (2001).
[30] K. Schmidt-Rohr and Q. Chen, Nat. Mater. **7**, 75 (2008).
[31] L. Rubatat, A. L. Rollet, G. Gebel, and O. Diat, Macromolecules **35**, 4050 (2002).
[32] L. Rubatat, G. Gebel, and O. Diat, Macromolecules **37**, 7772 (2004).
[33] G. Gebel and O. Diat, Fuel Cells **5**, 261 (2005).
[34] B. Loppinet and G. Gebel, Langmuir **14**, 1977 (1998).
[35] G. Alberti, R. Narducci, and M. Sganappa, J. Power Sources **178**, 575 (2008).
[36] X. Kong and K. Schmidt-Rohr, Polymer **52**, 1971 (2011).
[37] G. Alberti, M. L. D. Vona, and R. Narducci, Int. J. Hydrogen Energy **37**, 6302 (2012).
[38] R. Hiesgen, S. Helmly, T. Morawietz, X.-Z. Yuan, H. Wang, and K. A. Friedrich, Electrochim. Acta **110**, 292 (2013).
[39] I. Nakamura and Z.-G. Wang, Soft Matter **9**, 5686 (2013).
[40] T. M. Birshtein, O. Borisov, Y. B. Zhulina, A. R. Khokhlov, and T. A. Yurasova, Polymer Sci. USSR **29**, 1293 (1987).
[41] P. A. Cirkel, T. Okada, and S. Kinugasa, Macromolecules **32**, 531 (1999).
[42] R. Koestner, Y. Roiter, I. Kozhinova, and S. Minko, Langmuir **27**, 10157 (2011).
[43] B. Rosi-Schwartz and G. R. Mitchell, Polymer **37**, 1857 (1996).
[44] E. Friedman, Circles in Circles, Erich's Packing Center (2012), www.stetson.edu.
[45] G. Lamm, in *Reviews in Computational Chemistry*, Vol. 19, edited by K. B. Lipkowitz, R. Larter, and T. R. Cundari (John Wiley & Sons, Inc., Hoboken, NJ, 2003), Chap. 4, p. 147.
[46] A. A. Kornyshev and S. Leikin, Phys. Rev. E **62**, 2576 (2000).
[47] S. J. Paddison, L. R. Pratt, and T. A. Zawodzinski, J. Phys. Chem. A **105**, 6266 (2001).
[48] G. Gebel and R. B. Moore, Macromolecules **33**, 4850 (2000).
[49] K. Kreuer, M. Schuster, B. Obliers, O. Diat, U. Traub, A. Fuchs, U. Klock, S. Paddison, and J. Maier, J. Power Sources **178**, 499 (2008).
[50] S. B. Hutchens and W. Zhen-Gang, J. Chem. Phys. **127**, 084912 (2007).
[51] P. Aldebert, B. Dreyfus, and M. Pineri, Macromolecules **19**, 2651 (1986).
[52] P. Aldebert, B. Dreyfus, G. Gebel, N. Nakamura, M. Pineri, and F. Volino, J. Phys. France **49**, 2101 (1988).
[53] B. Loppinet, G. Gebel, and C. E. Williams, J. Phys. Chem. B **101**, 1884 (1997).
[54] E. Szajdzinska-Pietek, S. Schlick, and A. Plonka, Langmuir **10**, 1101 (1994).
[55] E. Szajdzinska-Pietek, S. Schlick, and A. Plonka, Langmuir **10**, 2188 (1994).
[56] R. Hiesgen (private communication) (2013).
[57] K.-D. Kreuer and G. Portale, Adv. Funct. Mater. **23**, 5390 (2013).
[58] S. S. Jang, V. Molinero, T. Çağın, and W. A. Goddard, J. Phys. Chem. B **108**, 3149 (2004).
[59] C. K. Knox and G. A. Voth, J. Phys. Chem. B **114**, 3205 (2010).
[60] P. V. Komarov, P. G. Khalatur, and A. R. Khokhlov, Beilstein J. Nanotechnol. **4**, 567 (2013).
[61] G. Marchand, P. A. Bopp, and E. Spohr, Zeitschrift Naturforschung **68**, 101 (2013).
[62] G. Gebel, S. Lyonnard, H. Mendil-Jakani, and A. Morin, J. Phys.: Condens. Matter **23**, 234107 (2011).
[63] K. Malek, M. Eikerling, Q. Wang, Z. Liu, S. Otsuka, K. Akizuki, and M. Abe, J. Chem. Phys. **129**, 204702 (2008).
[64] K. Morohoshi and T. Hayashi, Polymers **5**, 56 (2013).
[65] D. Y. Galperin and A. R. Khokhlov, Macromolec. Theory Simul. **15**, 137 (2006).
[66] J. T. Wescott, Q. Yue, L. Subramanian, and T. Weston Capehart, J. Chem. Phys. **124**, 134702 (2006).